

Phase-field simulations of the effect of temperature and interface for zirconium δ-hydrides

Zi-Hang Chen(陈子航), Jie Sheng(盛杰), Yu Liu(刘瑜), Xiao-Ming Shi(施小明), Houbing Huang(黄厚兵), Ke Xu(许可), Yue-Chao Wang(王越超), Shuai Wu(武帅), Bo Sun(孙博), Hai-Feng Liu(刘海风), and Hai-Feng Song(宋海峰)

Citation: Chin. Phys. B, 2024, 33 (**4**): 048201. DOI: 10.1088/1674-1056/ad1f4d
Journal homepage: http://cpb.iphy.ac.cn; http://iopscience.iop.org/cpb

What follows is a list of articles you may be interested in

Concerted versus stepwise mechanisms of cyclic proton transfer: Experiments, simulations, and current challenges

Yi-Han Cheng(程奕涵), Yu-Cheng Zhu(朱禹丞), Xin-Zheng Li(李新征), and Wei Fang(方为)
Chin. Phys. B, 2023, 32 (**1**): 018201. DOI: 10.1088/1674-1056/ac98a5

Adaptive semi-empirical model for non-contact atomic force microscopy

Xi Chen(陈曦), Jun-Kai Tong(童君开), and Zhi-Xin Hu(胡智鑫)
Chin. Phys. B, 2022, 31 (**8**): 088202. DOI: 10.1088/1674-1056/ac6eec

Theoretical study on the exciton dynamics of coherent excitation energy transfer in the phycoerythrin 545 light-harvesting complex

Xue-Yan Cui(崔雪燕), Yi-Jing Yan(严以京), and Jian-Hua Wei(魏建华)
Chin. Phys. B, 2022, 31 (**1**): 018201. DOI: 10.1088/1674-1056/ac0bad

Driven injection of a polymer into a spherical cavity: A Langevin dynamics simulation study

Chao Wang(王超), Fan Wu(吴凡), Xiao Yang(杨肖), Ying-Cai Chen(陈英才), and Meng-Bo Luo(罗孟波)
Chin. Phys. B, 2021, 30 (**10**): 108202. DOI: 10.1088/1674-1056/abff21

Theoretical investigation on the excited state intramolecular proton transfer in Me_2N substituted flavonoid by the time-dependent density functional theory method

Hang Yin(尹航), Ying Shi(石英)
Chin. Phys. B, 2018, 27 (**5**): 058201. DOI: 10.1088/1674-1056/27/5/058201

Phase-field simulations of the effect of temperature and interface for zirconium δ-hydrides

Zi-Hang Chen(陈子航)[1,2,3,†], Jie Sheng(盛杰)[3,†], Yu Liu(刘瑜)[3,‡], Xiao-Ming Shi(施小明)[4], Houbing Huang(黄厚兵)[1,2], Ke Xu(许可)[1,2,3], Yue-Chao Wang(王越超)[3], Shuai Wu(武帅)[1,2,3], Bo Sun(孙博)[3], Hai-Feng Liu(刘海风)[3], and Hai-Feng Song(宋海峰)[3]

[1] *School of Materials Science and Engineering, Beijing Institute of Technology, Beijing* 100081, *China*
[2] *Advanced Research Institute of Multidisciplinary Science, Beijing Institute of Technology, Beijing* 100081, *China*
[3] *Laboratory of Computational Physics, Institute of Applied Physics and Computational Mathematics, Beijing* 100088, *China*
[4] *Department of Physics, University of Science and Technology Beijing, Beijing* 100083, *China*

(Received 25 November 2023; revised manuscript received 4 January 2024; accepted manuscript online 17 January 2024)

Hydride precipitation in zirconium cladding materials can damage their integrity and durability. Service temperature and material defects have a significant effect on the dynamic growth of hydrides. In this study, we have developed a phase-field model based on the assumption of elastic behaviour within a specific temperature range (613 K–653 K). This model allows us to study the influence of temperature and interfacial effects on the morphology, stress, and average growth rate of zirconium hydride. The results suggest that changes in temperature and interfacial energy influence the length-to-thickness ratio and average growth rate of the hydride morphology. The ultimate determinant of hydride orientation is the loss of interfacial coherency, primarily induced by interfacial dislocation defects and quantifiable by the mismatch degree q. An escalation in interfacial coherency loss leads to a transition of hydride growth from horizontal to vertical, accompanied by the onset of redirection behaviour. Interestingly, redirection occurs at a critical mismatch level, denoted as q_c, and remains unaffected by variations in temperature and interfacial energy. However, this redirection leads to an increase in the maximum stress, which may influence the direction of hydride crack propagation. This research highlights the importance of interfacial coherency and provides valuable insights into the morphology and growth kinetics of hydrides in zirconium alloys.

Keywords: zirconium hydride, phase-field method, temperature effect, mismatch degree

PACS: 82.20.Wt, 81.30.–t, 05.70.Np **DOI:** 10.1088/1674-1056/ad1f4d

1. Introduction

Zirconium (Zr) alloys are extensively employed as cladding materials in various reactor types[1] due to their low neutron absorption rate, robust resistance to corrosion, and adequate high temperature strength, excellent thermal conductivity, and ductility.[2,3] However, hydrogen is absorbed into the Zr cladding by the waterside corrosion reaction during reactor operation,[4] thereby precipitating hydrides when the solid solubility limit of the hydrogen in the Zr alloys is exceeded. Hydride precipitates causes a degradation in the mechanical properties of the cladding,[5] increasing the embrittlement and even inducing the fracture of the cladding.[3,6] Consequently, the investigation of the hydrogen corrosion behavior in Zr is crucial for predicting material property degradation and assessing the service life of the cladding.

A great deal of experimental works have been done to better understand hydride precipitate and growth in Zr alloys.[6] Based on experiments,[7–9] there are four recognized phases of hydrides which can form in Zr, namely, ζ-$ZrH_{0.5}$, γ-ZrH, δ-$ZrH_{1.5+x}$, and ε-ZrH_2 phases. The δ-phase is a stable face-centered cubic (fcc) phase and the most prevalent phase in the cladding materials. The δ-hydrides usually form on the circumferential planes of cladding in the absence of stresses, and have a platelet-like shape.[10,11] Moreover, when the cladding with hydrides is subjected to high temperature (350 °C for example) and applied tensile circumferential stress during dry storage, these hydride platelets undergo a transition from circumferential to radial orientations relative to the cladding tube geometry by dissolving and precipitating.[12–14] The reoriented radial hydrides serve as fracture initiators and propagation, and ultimately cause the mechanical failure of the cladding. Therefore, the mechanical properties and performance of the Zr cladding are highly sensitive to the specific hydride microscopic morphology. However, more information is still needed in the areas of the formation mechanisms of various hydride morphology, particularly to develop the capability to simulate accurately these various morphologies under varying conditions, such as different temperatures.

Phase-field (PF) modeling, based on principles of thermodynamics and kinetics, provides a powerful approach for simulating microstructure evolution in various phase transformation phenomena, such as spinodal decomposition,[15,16]

[†]These authors contributed equally to this work.
[‡]Corresponding author. E-mail: liu_yu@iapcm.ac.cn

© 2024 Chinese Physical Society and IOP Publishing Ltd

coarsening,[17,18] solidification,[19–21] and film growth.[22–25] Numerous PF models have been developed to investigate the microstructure evolution of different hydrides in Zr alloys. Most of them were created for the ζ-hydride[26–28] and the γ-hydride.[29–34] In recent years, many researchers have focused on the δ-hydrides and started to develop corresponding PF models to study the characteristics of δ-hydride morphology. Jokisaari *et al.*[35] developed a δ-hydride PF model to study the growth kinetics of the δ-hydride by modifying the free energies based on the CALPHAD (CALculation of PHAse Diagrams). Bair *et al.*[36] investigated the effects of metastable phases (ζ-phase and γ-phase) on the nucleation and growth of the δ-hydride using a multiphase-field model. Han *et al.*[10] explored the stacking structure formation and transition of δ-hydride precipitates in Zr. Heo *et al.*[11] developed a polycrystalline PF model considering the loss of the interfacial coherency and the grain boundary segregation to investigate δ-hydride growth behavior. Additionally, Lin *et al.*[37] and Shin *et al.*[38] examined the reorientation behavior of δ-hydrides under applied stress fields. Simon *et al.*[39] developed a quantitative PF model for δ-hydrides and analyzed the role of anisotropic elastic interaction on hydride stacking and reorientation. Wu *et al.*[40] studied the microstructural evolution of hydride blister formed by δ-hydride aggregation. However, the morphology and growth kinetics of δ-hydride are strongly influenced by the environmental temperature and metal/hydride interfacial effects (interfacial energy and interfacial coherency). Previous studies on δ-hydrides in Zr lacked detailed discussion on the these key factors governing δ-hydride morphology and growth kinetics, hindering the accurate simulation of δ-hydride morphology in Zr and the development of quantitative PF model. Therefore, it is imperative to explore and comprehend the influences of these factors on δ-hydride morphology and growth behavior in Zr.

This work aims to investigate the influence of temperature and interfacial effects on the δ-hydride morphology and growth kinetics. To achieve this objective, we adopt a PF model based on the Kim–Kim–Suzuki (KKS) assumption.[41] Using CALPHAD method, temperature-dependent bulk free energy curves are constructed to describe the contribution of bulk free energy to the total free energy within the service temperature range of zirconium alloys. Therefore, we can capture the morphological changes of hydrides at different temperatures. In addition, the effects of interfacial energy and the loss of interfacial coherency on the morphology, stress and growth kinetics of hydrides are studied, and a reorientation behavior influenced by the loss of interfacial coherency is found. Meanwhile, we reveal the underlying mechanism of these factors affecting the hydride morphology and growth kinetics based on the diffusion interfacial velocity theory.

The contents of the article are organized as follows. In Section 2, we presents this PF model coupled with varying temperature in detail, including the governing equations of the PF model and the free energies of the system and the interface moving velocity. In Section 3, the results and their implications are presented. Finally, Section 4 includes the paper by summarizing the key results and contributions of this study.

2. Phase-field model

2.1. Governing equation

The PF method is widely used to study the evolution of microstructures with heterogeneity in composition and structure. Specifically, in the Zr–H system, the structural order parameter η is used to describe the phase transformation from α-Zr matrix to δ-hydride precipitate and the variation of hydrogen concentration c is used to describe diffusion during the phase transformation. In this PF model, the Zr–H system's total free energy F is consist of the bulk free energy F_{bulk}, the interface gradient energy F_{int}, and the elastic strain energy F_{el}, which is given by

$$\begin{aligned} F &= F_{\text{bulk}} + F_{\text{int}} + F_{\text{el}} \\ &= \int \left[f_{\text{bulk}}(c,T,\eta) + f_{\text{int}}(\nabla\eta,\nabla c) + f_{\text{el}}(\boldsymbol{u},\eta) \right] \mathrm{d}V, \end{aligned} \tag{1}$$

where $f_{\text{bulk}}(c,T,\eta)$ is the bulk free energy density as a function of temperature T, composition c, and structural order parameter η, $f_{\text{int}}(\nabla\eta,\nabla c)$ is the interface gradient energy density because of diffuse interface, $f_{\text{el}}(\boldsymbol{u},\eta)$ is the elastic strain energy density associated with displacement $\boldsymbol{u}$ and order parameter η.

To ensure the reduction of the free energy during the evolution of microstructures, the PF governing equation could be derived by minimizing the total free energy F via variational differentiation as follows:

$$\frac{\partial \eta}{\partial t} = -M\frac{\delta F}{\delta \eta}, \tag{2}$$

$$\frac{\partial c}{\partial t} = \nabla \cdot \left(D\nabla \frac{\delta F}{\delta c} \right), \tag{3}$$

where M is the kinetic coefficient, t is time, D is the mobility similar to one defined by Steinbach and Apel as follows:[42] $D = D_0/(\partial^2 f_{\text{bulk}}/\partial c^2)$, where D_0 is the diffusion coefficient.

2.2. Bulk free energy density

The bulk free energy density can be constructed by KKS assumption. In the KKS assumption, each material point is regarded as a mixture of two phases, and a local equilibrium of chemical potential is always satisfied between the two phases. In this PF model, these assumptions could be expressed as follows:

$$c = [1-h(\eta)]c_\alpha + h(\eta)c_\delta, \tag{4}$$

$$\frac{\partial f_\alpha(c_\alpha,T)}{\partial c_\alpha} = \frac{\partial f_\delta(c_\delta,T)}{\partial c_\delta}, \tag{5}$$

where c_α and c_δ are the mole fraction of hydrogen in the α-Zr matrix and δ-hydride precipitate respectively; $f_\alpha(c_\alpha, T)$ and $f_\delta(c_\delta, T)$ are the free energy densities of the α-Zr matrix and δ-hydride precipitate at temperature T respectively. Additionally, $h(\eta) = 3\eta^2 - 2\eta^3$ is the interpolation function that increases monotonically from $h(\eta = 0) = 0$ to $h(\eta = 1) = 1$. The bulk free energy density $f_{\text{bulk}}(c, T, \eta)$ of the system is defined by a method similar to the concentration assumption as follows:

$$f_{\text{bulk}}(c,T,\eta) = h(\eta) f_\delta(c_\delta,T) + [1-h(\eta)] f_\alpha(c_\alpha,T) + wg(\eta), \tag{6}$$

$$f_\alpha(c_\alpha,T) = \frac{G_{\text{m}}^\alpha}{V_{\text{m}}}, \tag{7}$$

$$f_\delta(c_\delta,T) = \frac{G_{\text{m}}^\delta}{V_{\text{m}}}, \tag{8}$$

where $g(\eta) = \eta^2(1-\eta^2)$ is the double potential well function and w is the height of the double potential well, G_{m}^α and G_{m}^δ are the molar Gibbs free energies of the α-Zr matrix and δ-hydride precipitate respectively; V_{m} is the molar volume of the system.

The molar Gibbs free energies G_{m}^α and G_{m}^δ can be obtained by CALPHAD method through the sublattice model.[43,44] In the sublattice model, Zr fills the first sublattice and hydrogen and vacancies fill the second sublattice. Considering the α-Zr matrix with an hcp structure and δ-hydride precipitate with an fcc structure, $(\text{Zr})_1(\text{H},\square)_1$ is used to describe the α-Zr matrix and $(\text{Zr})_1(\text{H},\square)_2$ is used to describe δ-hydride precipitate. The molar free energies for α-Zr and δ-hydride is expressed by the following formula:

$$G_{\text{m}}^\alpha = G_{\text{m}}^{\text{ref},\alpha} + G_{\text{m}}^{\text{mix},\alpha}, \tag{9}$$

$$G_{\text{m}}^\delta = G_{\text{m}}^{\text{ref},\delta} + G_{\text{m}}^{\text{mix},\delta} + G_{\text{m}}^{\text{ex},\delta}, \tag{10}$$

$$G_{\text{m}}^{\text{ref},\alpha} = \frac{1}{1+y_{\text{H}}}\left(y_{\text{H}} G_{\text{Zr:H}}^{0,\alpha} + y_\square G_{\text{Zr:}\square}^{0,\alpha}\right), \tag{11}$$

$$G_{\text{m}}^{\text{mix},\alpha} = \frac{1}{1+y_{\text{H}}} RT\left(y_{\text{H}} \ln y_{\text{H}} + y_\square \ln y_\square\right), \tag{12}$$

$$G_{\text{m}}^{\text{ref},\delta} = \frac{1}{1+2y_{\text{H}}}\left(y_{\text{H}} G_{\text{Zr:H}}^{0,\delta} + y_\square G_{\text{Zr:}\square}^{0,\delta}\right), \tag{13}$$

$$G_{\text{m}}^{\text{mix},\delta} = \frac{2}{1+2y_{\text{H}}} RT\left(y_{\text{H}} \ln y_{\text{H}} + y_\square \ln y_\square\right), \tag{14}$$

$$G_{\text{m}}^{\text{ex},\delta} = \frac{1}{1+2y_{\text{H}}} y_{\text{H}} y_\square \left[L_{\text{Zr:H},\square}^{0,\delta} + L_{\text{Zr:H},\square}^{1,\delta}(y_{\text{H}} - y_\square)\right], \tag{15}$$

where $G_{\text{m}}^{\text{ref},\alpha}$ and $G_{\text{m}}^{\text{ref},\delta}$ are the reference free energy of mixing of the end members in the α-Zr matrix and δ-hydride precipitate respectively; $G_{\text{m}}^{\text{mix},\alpha}$ and $G_{\text{m}}^{\text{mix},\delta}$ are the free energy of mixing for an ideal soluation in the α-Zr matrix and δ-hydride precipitate respectively. Significantly, the free energy formula of δ-hydride precipitate compared with the matrix includes the excess free energy $G_{\text{m}}^{\text{ex},\delta}$ of mixing. The parameters for $G_{\text{Zr:H}}^{0,\alpha}$, $G_{\text{Zr:}\square}^{0,\alpha}$, $G_{\text{Zr:H}}^{0,\delta}$, $G_{\text{Zr:}\square}^{0,\delta}$, $L_{\text{Zr:H},\square}^{0,\delta}$, $L_{\text{Zr:H},\square}^{1,\delta}$ are supplied by Refs. [43,44]. y_{H} and $y_\square$ are the mole fractions of hydrogen and vacancy atom related to c_α and c_δ respectively. These formulas for the α-Zr matrix can be expressed as follows:

$$y_{\text{H}} = \frac{c_\alpha}{1-c_\alpha}, \tag{16}$$

$$y_\square = 1 - \frac{c_\alpha}{1-c_\alpha}. \tag{17}$$

These formulas for the δ-hydride precipitate can be expressed as follows:

$$y_{\text{H}} = \frac{c_\delta}{2(1-c_\delta)}, \tag{18}$$

$$y_\square = 1 - \frac{c_\delta}{2(1-c_\delta)}. \tag{19}$$

According to the above CALPHA method, the Zr–H phase diagram is drawn in Fig. 1. To improve the numerical stability of the calculation, the molar Gibbs free energies G_{m}^α and G_{m}^δ are approximated by using quadratic polynomials near the equilibrium composition. Based on parabola approximation,[36,45,46] the molar Gibbs free energies G_{m}^α and G_{m}^δ are written as

$$G_{\text{m}}^\alpha = a_1(T) c_\alpha^2 + b_1(T) c_\alpha + c_1(T), \tag{20}$$

$$G_{\text{m}}^\delta = a_2(T) c_\delta^2 + b_2(T) c_\delta + c_2(T), \tag{21}$$

$$a_1(T) = 206.6\text{e}^{4429/T}\ (\text{J/mol}), \tag{22}$$

$$b_1(T) = 40.63T - 8.918\times10^4\ (\text{J/mol}), \tag{23}$$

$$c_1(T) = -55.56T + 6484\ (\text{J/mol}), \tag{24}$$

$$a_1(T) = -771.3T + 8.305\times10^5\ (\text{J/mol}), \tag{25}$$

$$b_1(T) = 1021T - 1.109\times10^6\ (\text{J/mol}), \tag{26}$$

$$c_1(T) = -361.2T + 3.216\times10^5\ (\text{J/mol}), \tag{27}$$

where the detail determined method of coefficients can be seen in Section 1 of supplementary materials.

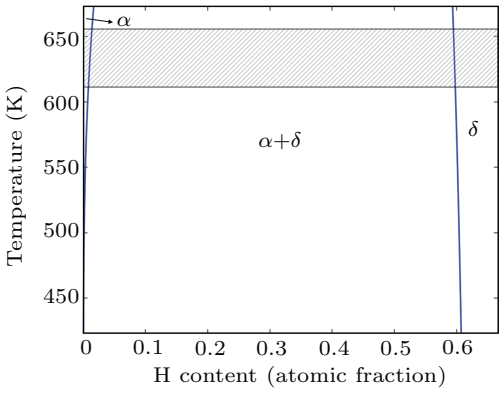


Fig. 1. The Zr–H phase diagram. The simulation test in this work is conducted in accordance with the service temperature range of the Zr cladding tube, with 613 K–653 K (shaded part of the fig) selected as the operating temperatures.

The service temperature of the Zr cladding tube is around 623 K. Figure 2 shows the results of the parabolic approximation for molar Gibbs free energies G_{m}^α and G_{m}^δ from $T = 613$ K to $T = 653$ K.

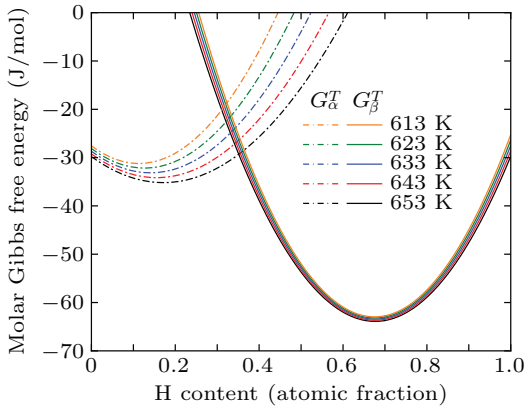


Fig. 2. Parabolic approximations for molar Gibbs free energies $G_{\rm m}^{\alpha}$ and $G_{\rm m}^{\delta}$ from $T = 613$ K to $T = 653$ K.

2.3. Interface gradient energy density

The interface gradient energy density includes two aspects of contribution from inhomogeneous composition and structure across the interface.[10,47] In the PF frame, the interface gradient density could be written as

$$f_{\rm int}(\nabla\eta, \nabla c) = \frac{1}{2}k_\eta^2 |\nabla\eta|^2 + \frac{1}{2}k_{\rm c}^2 |\nabla c|^2, \tag{28}$$

where k_η^2 and $k_{\rm c}^2$ are the gradient energy coefficients related to the order parameter gradient and the concentration gradient, respectively. Due to the fact that the contribution of order parameter gradient to the interface gradient energy could be sufficient to approximate the energy contribution from the diffuse interface, so it is assumed that $k_{\rm c}^2 = 0$.[10,47]

The value of gradient energy coefficient k_η^2 and the height of the double potential well w could be determined by interfacial energy σ and interface thickness λ, as follows:[48]

$$k_\eta^2 = \frac{3}{4}\sigma\lambda, \tag{29}$$

$$w = 24\frac{\sigma}{\lambda}. \tag{30}$$

2.4. Elastic strain energy density

Due to lattice mismatch and volume mismatch of two phases during the phase transformation from α-Zr matrix to δ-hydride precipitate, the elastic strain energy generated can not be ignored. The elastic strain energy density $f_{\rm el}$ is expressed as

$$f_{\rm el}(\boldsymbol{u}, \eta) = \frac{1}{2}C_{ijkl}\varepsilon_{ij}^{\rm el}\varepsilon_{kl}^{\rm el}, \tag{31}$$

where $\varepsilon_{ij}^{\rm el}$ is the elastic strain, C_{ijkl} is the elastic constant tensor (the Einstein summation convention is used). Because solving the elastic solution of elastic inhomogeneous solid requires a lot of calculations, in our simulation, we assume that the elastic constant of the hydride phase is the same as that of the matrix.[10] According to the classical Khachaturyan micro-elasticity theory,[49] the elastic strain can be calculated as follows:

$$\varepsilon_{ij}^{\rm el} = \delta\varepsilon_{ij} - \varepsilon_{ij}^{00}(q)h(\eta), \tag{32}$$

$$\delta\varepsilon_{ij} = \frac{1}{2}\left(\frac{\partial u_i}{\partial x_j} + \frac{\partial u_j}{\partial x_i}\right), \tag{33}$$

where $\delta\varepsilon_{ij}$ is the microscopic heterogeneous strain relates to the displacement $\boldsymbol{u}$. $\varepsilon_{ij}^{00}(q)$ is the eigenstrain related to the mismatch degree q, depicting the degree of lattice mismatch due to the volume expansion during the phase transformation and the loss of interfacial coherency. The mismatch degree q describes the loss degree of interfacial coherency. Notably, only elastic strain is taken into account in this PF model, which means that no plastic deformation could take place.

With Lagrangian finite-strain theory,[50] the eigenstrain is expressed as

$$\varepsilon_{ij}^{00}(q) = \frac{1}{2}\left(F^{\rm T}F - I\right), \tag{34}$$

$$F = \left(\frac{1}{q}\right)^{1/3} \cdot \begin{bmatrix} \dfrac{(\sqrt{2}/2)a_\delta}{a_\alpha} & 0 & 0 \\ 0 & q\cdot\dfrac{(2\sqrt{3}/3)a_\delta}{c_\alpha} & 0 \\ 0 & 0 & \dfrac{(\sqrt{2}/2)a_\delta}{a_\alpha} \end{bmatrix}, \tag{35}$$

where F is the total lattice transformation tensor or deformation gradient tensor,[11] the superscript T represents the matrix transpose and I represents the identity matrix, a_α, c_α, and a_δ represents the lattice parameters of α-Zr and δ-hydride. The calculation process of F is detailed in Section 2 of supplementary materials. Noted that shear component is not included in the total lattice transformation tensor, as the δ-hydride formation path calculated by Louche*et al.*[51] and Zhang*et al.*[52] shows that the total energy without considering the shear component is lowest and more favorable. Therefore, we did not introduce the shear component in the simulation, and Simon[39] used a similar approach in the simulation.

Once the elastic constant tensor and strain are defined, the stress σ_{ij} assuming linear elasticity is derived as follows:

$$\sigma_{ij} = C_{ijkl}\varepsilon_{kl}^{\rm el}. \tag{36}$$

The displacement of system is obtained by assuming the use of quasi steady state approximation to solve the mechanical equilibrium equation, as follows:

$$\nabla\cdot\sigma_{ij} = 0. \tag{37}$$

2.5. Interface moving velocity

In the classical sharp interface kinetics, the normal moving velocity of the interface is proportional to the variation of free energy per unit volume during the nucleation and growth process.[54] For the PF diffuse interface kinetics, Yang *et al.*[48] adopted the operator analysis method to analyze the PF kinetics equation, and derived the expression of the interface moving velocity. The specific expression is as follows:

$$v_{\rm int} = \frac{3}{4}M\lambda\left(\Delta G - \sigma H_{\rm curv}\right), \tag{38}$$

$$\Delta G = \Delta G_{\text{chem}} - \Delta G_{\text{el}}, \tag{39}$$

$$\Delta G_{\text{chem}} = f_\alpha(c_\alpha, T) - f_\delta(c_\delta, T) - \frac{\partial f_\alpha(c_\alpha, T)}{\partial c_\alpha}(c_\alpha - c_\delta), \tag{40}$$

$$\Delta G_{\text{el}} = -\sigma_{ij}\varepsilon_{ij}^{00}(q), \tag{41}$$

where H_{curv} represents the local curvature, ΔG represents the change of free energy during the phase transformation, including two parts: chemical driving force ΔG_{chem} and elastic interaction energy ΔG_{el}. It can be seen from the above formula that the interface moving velocity is mainly affected by the dynamic coefficient, interfacial energy, chemical driving force, elastic interaction energy, and interface curvature. In Eq. (38), the first term promotes the occurrence of the movement of the interface, and the second term inhibits the advancement of the interface, and the smaller the radius of curvature, the more obvious the inhibition effect. When the elastic interaction energy (ΔG_{el}) is negative, it exerts a positive influence on interface pushing. Conversely, when ΔG_{el} is positive, it exhibits an inhibitory effect on interface pushing.[10]

2.6. Numerical implementation

In this study, the finite element method (FEM)[34,35] is used to solve the governing equation. To ensure both stability and accuracy in the numerical simulations, a triangular element with a grid size of 2 nm is chosen. Additionally, a local adaptive mesh refinement scheme is applied strategically to avoid unnecessary refinement of finite element meshes throughout the simulation domain, thus enhancing computational efficiency.

For time integration, we adopt the implicit backward difference method, which provides numerical stability when solving the time-dependent governing equation. To further optimize the time stepping process, an adaptive time marching scheme is implemented with a tolerance level set at 10^{-3}. This adaptive approach allowed for efficient time stepping while still maintaining the required level of accuracy for the simulation results.

3. Results and discussion

The initial hydrogen concentration in the matrix is set to 0.05, while the hydride has an initial concentration of 0.6.[10] Nucleation of the hydride occurres at the center of the simulation domain, with a nucleation point having a radius of 2 nm. The presence of hydrogen in the matrix at a supersaturated level serves as a larger driving force for hydride growth,[10] ultimately reaching a two-phase equilibrium. Table 1 provides an overview of all the parameters utilized in this simulation.

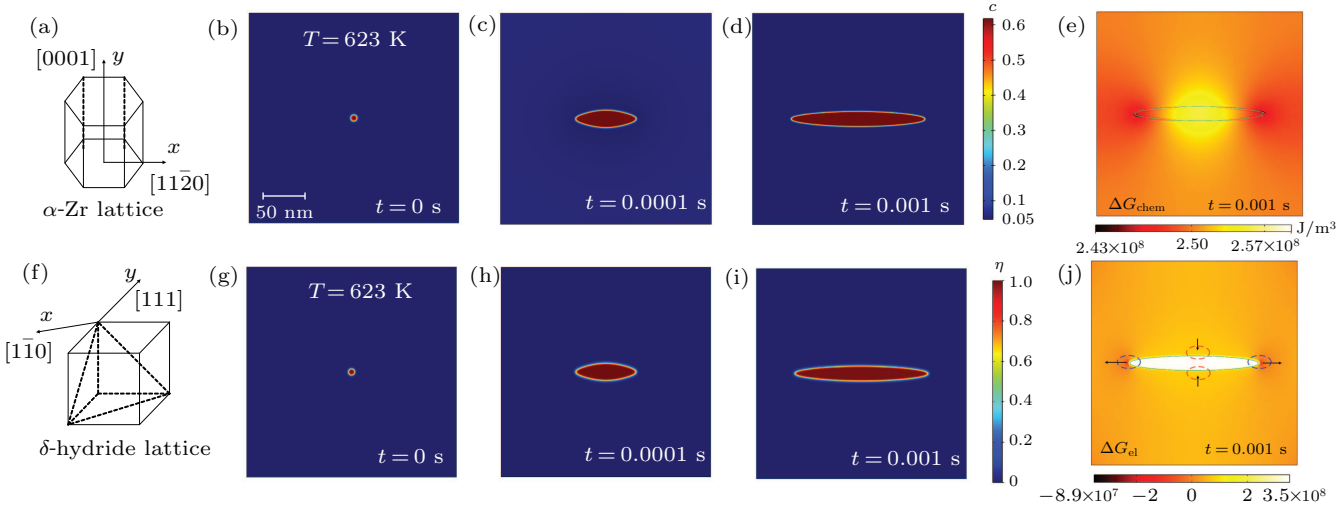


Fig. 3. Coordinate system for hcp α-Zr lattice (a) and δ-hydride lattice (f). Evolution of c (b), (c), (d) and η (g), (h), (i) as a function of time for systems, a single h.c.p Zr crystal describes the crystalline orientation of the system (The mismatch degree q is equal to 1). (e) Distribution diagram of chemical driving force of δ-hydrfide. (g) Distribution diagram of elastic interaction energy of δ-hydride.

To validate the effectiveness of the model, we initially conducted tests under completely coherent conditions with a mismatch degree of $q = 1$, consistent with previous results. These tests confirmed the reliability and accuracy of our model in capturing the growth morphology of hydrides. As illustrated in Figs. 3(b)–3(d) and 3(g)–3(i), the phase transformation from the metal matrix to hydride precipitation has been effectively monitored and characterized using variables c (concentration) and η (order parameter). In Figs. 3(a) and 3(f), the system orientation is specified such that the x axis (horizontal direction) and the y axis (vertical direction) align with the a axis ($\{11\bar{2}0\}_\alpha$ direction) and c axis ($\{0001\}_\alpha$ direction) of a hcp Zr crystal. Due to the mismatch of the hydride phase being greater along the a-axis direction than along the c-axis direction, hydride growth predominantly occurs in the a-axis direction, resulting in an elliptical shape of the hydride particles.

The energy distribution analysis of the hydride, illustrated in Figs. 3(e) and 3(j), reveals a relatively uniform distribution

of the chemical driving force, with slightly lower values observed at the hydride tip. In contrast, the distribution of elastic interaction energy exhibits greater anisotropy compared to the chemical driving force. At the hydride tip, the negative elastic interaction energy favors hydride growth along the a axis. The positive elastic interaction energy can inhibit hydride growth along the c axis. These results highlight the important role of elastic interaction energy in shaping hydride morphology. Next, the effects of temperature, interfacial energy and mismatch degree on the kinetic growth of hydride were tested.

3.1. Effect of temperature

Hydrogen can exist as a solvent in the zirconium matrix. However, the presence of excess hydrogen or changes in temperature can lead to the precipitation of hydrides.[34,55] To investigate the effect of temperature on δ-hydride, simulations were performed with consistent initial conditions at temperatures of 613 K, 623 K, 633 K, 643 K, and 653 K. The focus was on investigating the influence of temperature on hydride shape and average growth rate.

Within this temperature range, the diffusion coefficient exhibits variations as a function of temperature, while no significant changes are observed in the elastic constants and eigenstrain.[37] For these reasons, all simulations were performed using the elastic constants, egienstrain and temperature dependent diffusion coefficients given in Table 1. Note that we do not consider the changes in interfacial energy and eigenstrain caused by the loss of interface coherency in this section.

The simulation results presented in Fig. 4(a) demonstrate the significant impact of temperature on the length and thickness of hydrides. The results are primarily due to effects in chemical free energy as a result of temperature changes. The length-to-thickness ratio of hydride initially increases and then decreases as the temperature rises. In addition, the evolution of the area of hydride over time at different temperatures and the average growth rate were depicted in Fig. 4(b). As the temperature increases, the area of hydride decreases, accompanied by a decrease in the growth rate. This decrease in the growth rate can be attributed to the reduction in the chemical driving force resulting from the increased temperature (as shown in Fig. 2, the temperature increases and G_α decreases).

Table 1. Model parameters used in the simulations.

Parameters	Symbol	Value	Unit
Interface thickness	λ	4×10^{-9}	m
Diffusion coefficient[10]	D_0	$7\times10^{-7}\mathrm{e}^{(-44560/RT)}$	m^2/s
Gas constant	R	8.3145	$\mathrm{J}/(\mathrm{mol}\cdot\mathrm{K})$
Molar volume[35]	V_m	14	$\mathrm{cm}^3/\mathrm{mol}$
Kinetic coefficients[10]	M	5×10^{-4}	$\mathrm{m}^3/(\mathrm{J}\cdot\mathrm{s})$
Elastic constant[53]	$C_{11},C_{12},C_{13},C_{33},C_{44}$	155, 67, 65, 155, 40	GPa
Eigenstrain[10]	ε_{ij}^{00}	$\frac{1}{2}\left(\left(\frac{1}{q}\right)^{2/3}\cdot\begin{bmatrix}1.07751 & 0 & 0\\ 0 & \left(\frac{1}{6}+\frac{4}{3}q^2\right)\cdot0.86821 & 0\\ 0 & 0 & 1.07751\end{bmatrix}-I\right)$	–
Misfit parameter[11]	q	0.8–1.0	–
Temperature	T	613–653	K
Interfacial energy[10]	σ	0.28–1.0	J/m^2

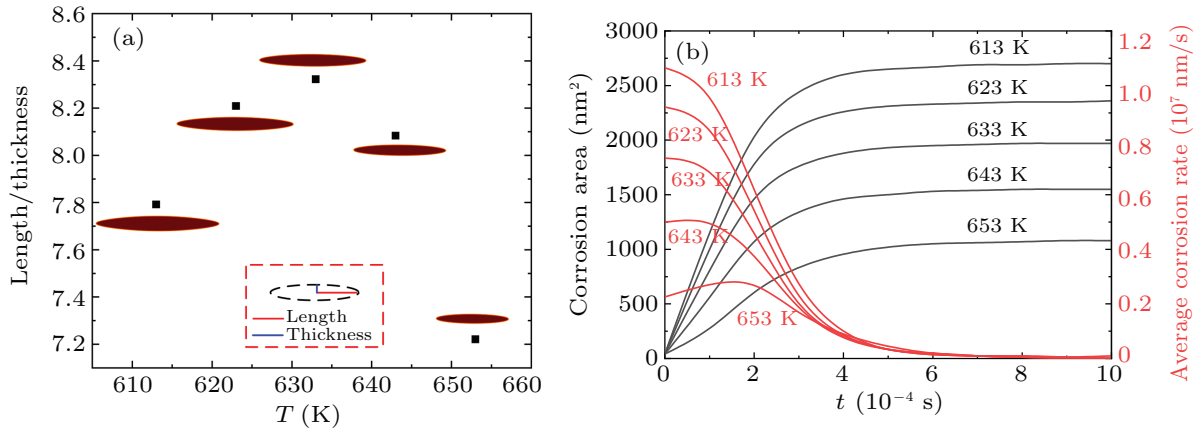


Fig. 4. (a) The length/thickness ratio of δ-hydride after 0.001-s evolution at different temperatures. (b) Area fraction of hydride phase and average growth rate at different temperatures.

3.2. Effect of interfacial energy

The loss of interfacial coherency between the hydride and matrix has a significant effect on the interfacial energy between α and δ phases. Jokisaari *et al.*[56] suggested that the interfacial energy includes the chemical energy of the interface and the energy contributed by the loss of interfacial coherency due to the existence of dislocations. Experimental and theoretical calculations have yielded different estimates for the α-δ coherent interfacial energy, with Jokisaari *et al.* reporting approximately 0.3 J/m^2, and Massih *et al.*[57] estimating it to be 0.28 J/m^2 from the measurement data of nucleation rate. However, the additional energy caused by the loss of interfacial coherency cannot be ignored. In this study, the range of interfacial energy caused by interfacial coherency loss was considered to be 0.28 J/m^2 to 1 J/m^2. The larger the interfacial energy, the larger the interfacial coherency loss. In addition, although Han *et al.*[10] have studied the morphology of δ-hydride under anisotropic interfacial energy, the results show that the anisotropic interfacial energy can only produce 1° torsion on the morphology of platelet hydride, and the key factor determining its morphology is the anisotropic eigenstrain. Therefore, the assumption of isotropic interfacial energy is adopted in our present study.

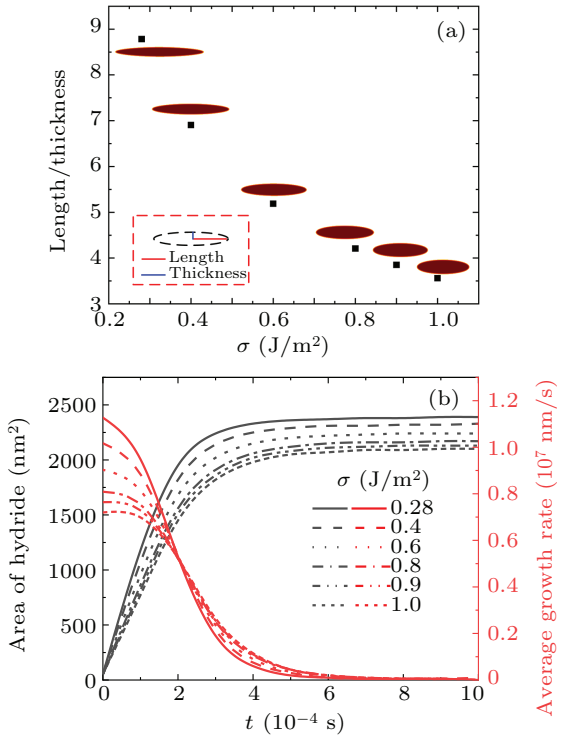


Fig. 5. (a) The length/thickness ratio of δ-hydride after 0.001-s evolution at different interfacial energies. (b) Area fraction of hydride phase and average growth rate at different interfacial energies.

As depicted in Fig. 5(a), the interfacial energy influences the morphology of the hydride. Higher values of interfacial energy lead to the formation of spherical hydrides rather than the platelet hydrides observed in experiments.[10,14] The hydride area and average growth rate changes over time under different interfacial energy conditions are illustrated in Fig. 5(b), indicating that the hydride area is larger under low interfacial energy. In terms of the growth rate, higher interfacial energy results in a slower growth rate of hydrides, and hydrides with lower interfacial energy reach equilibrium faster. The interfacial energy affects the gradient energy coefficient in the PF model and hinders the interfacial movement, which is consistent with the simulation results based on Eq. (38).

3.3. Effect of the loss of interfacial coherency

Due to the difference in crystal structure between the α-Zr matrix and the δ-hydride, hydride formation involves significant volume expansion, which usually results in the formation of dislocations due to adaptation to volume changes. Liu*et al.*[58] highlighted in their experiments that dislocations can induce lattice mismatch between two phases, resulting in a loss of interfacial coherency. In addition to the interfacial energy, the eigenstrain change caused by the loss of interfacial coherency is a more critical factor. In this section we will consider the effects of eigenstrain on hydride morphology, average growth rate and stress. We consider the mismatch degree introduced by Heo *et al.*[11] to describe the effect of interfacial coherency loss on the eigenstrain, as shown in Eq. (35).

The morphology of hydrides was simulated within the range of mismatch degrees from 0.8 (incompletely coherent interface) to 1 (fully coherent interface), as shown in Fig. 6(a). The length-to-thickness ratio of hydrides initially exhibits a decrease, followed by an increase as interfacial coherency loss escalates. When q exceeds 0.91, hydrides undergo redirection behavior and we designate this threshold as the critical mismatch degree q_c. This behavior can be elucidated by the anisotropic distribution of elastic interaction energy within hydrides due to the loss of interfacial coherency. As depicted in Fig. 6(b), with a decreasing q value, the elastic interaction energy initially exhibits an increase, followed by a decrease. When q exceeds q_c, the elastic interaction energy in both horizontal and vertical directions is positive, which hinders hydride growth. Nevertheless, the elastic interaction energy in the horizontal direction is lower than that in the vertical direction, indicating that the inhibitory effect in the horizontal direction is comparatively less pronounced than in the vertical direction. Consequently, hydrides tend to grow horizontally. At q_c, the elastic interaction energy in the two directions becomes equal, resulting in the formation of almost round hydrides. Conversely, when $q < q_c$, the horizontal elastic interaction energy is greater than the vertical elastic interaction energy, and the vertical elastic interaction energy is more favourable for the vertical growth of hydride, and when $q < 0.86$, the vertical elastic interaction energy is negative, and the vertical growth of hydride is more favourable. Addition-

ally, as the degree of mismatch increases, the average growth rate initially increases and then slows down, reaching its maximum value at q_c, corresponding to the minimum length-to-thickness ratio of hydride morphology. The average growth rate of the hydride has an opposite trend to the elastic interaction energy in both vertical and horizontal directions, which is consistent with the effect of the elastic interaction energy on the interface moving velocity in Eq. (38). From Fig. 6(c), we can visually observe the changes in the principal strain as the mismatch parameter decreases. When the strain in the 11 direction exceeds that in the 22 direction, hydrides exhibit a propensity to grow in the 11 direction. This provides a model-based explanation for the occurrence of reorientation.

From the perspective of stress distribution, the principal stresses σ_{xx} and σ_{yy} exhibit negative values within the interior of the hydrogen precipitates, reaching maximum values at the tips in Figs. 7(a) and 7(b). As depicted in Figs. 7(c) and 7(d), a reduction in the mismatch degree results in an increase in the maximum stress value. In addition, the redirection caused by the change in mismatch causes the change in σ_{xx} and σ_{yy} curves to reverse. Initially, σ_{xx} increases with distance along the x direction (solid line in Fig. 7(c)) and then stabilises, while σ_{xx} begins to increase along the y direction (dotted line in Fig. 7(c)) and then decreases with distance. Our simulation results show that the redirection causes changes in the stress and its maximum value. The change in stress can lead to a change in the direction of crack propagation at the hydride tip.

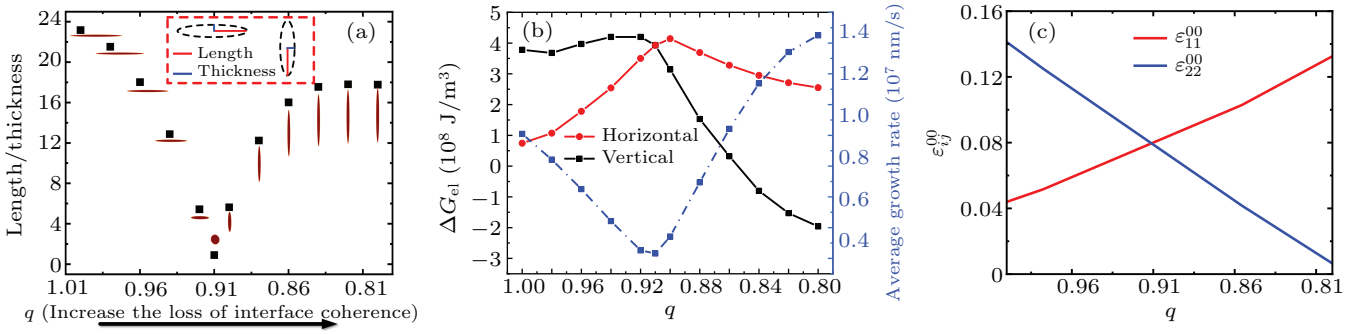


Fig. 6. (a) The morphology and length-to-thickness ratio of hydrides under varying mismatch conditions. (b) The average growth rate in both horizontal and vertical directions, along with the corresponding elastic interaction energy (represented by the red dot in the horizontal direction and the black dot in the vertical direction at the interface at time $t = 0.0002$ s) at different mismatch levels. (c) Eigenstrain at various mismatch levels.

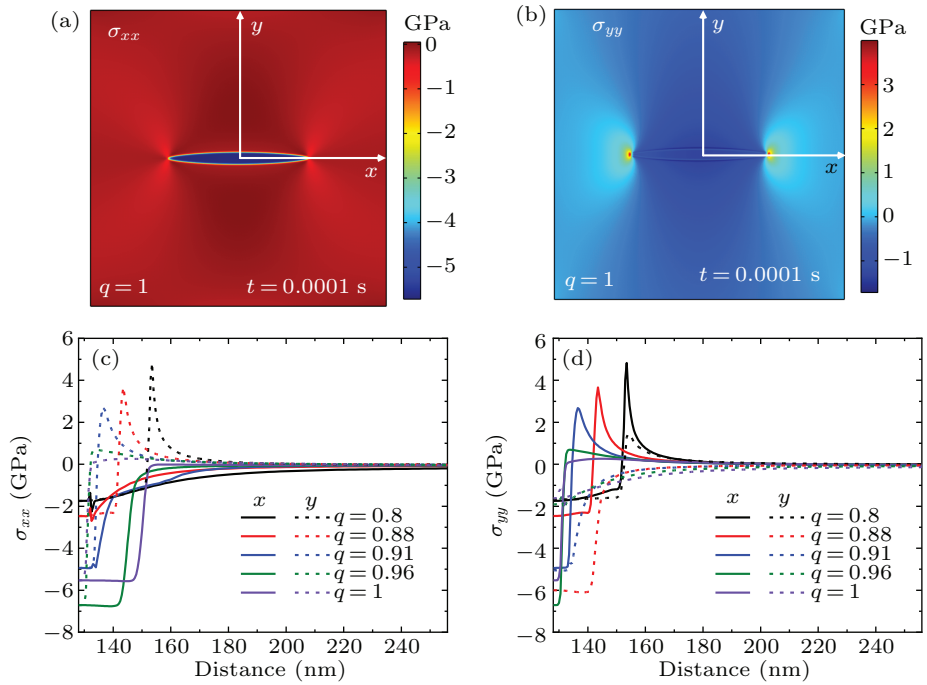


Fig. 7. (a) Distribution of principal stress σ_{xx}, (b) distribution of principal stress σ_{yy}, (c) σ_{xx} curves along the x and y directions under different mismatch values, (d) σ_{yy} curves along the x and y directions under different mismatch values.

To further examine the impact of temperature and interfacial energy on the mismatch degree in interfacial effects, we investigate the changes in the length-to-thickness ratio and elastic interaction energy distribution of hydrides at different mismatch degrees and temperatures (613 K, 623 K, and 633 K). Additionally, we analyze the length-to-thickness ra-

tio and elastic interaction energy distribution of hydrides under an interfacial energy value of 0.28 J/m^2, 0.5 J/m^2, and 0.8 J/m^2. The results from Figs. 8(a) and 8(b) illustrate that temperature influences the length-to-thickness ratio of hydrides at various mismatch degrees, while the overall trend of the length-to-thickness ratio remains consistent. Notably, the smallest length-to-thickness ratio of hydrides is consistently observed at a mismatch degree of q_c. Similarly, the analysis from Figs. 8(c) and 8(d) reveals that interfacial energy does not significantly impact the redirection of hydrides or the change trend of elastic interaction energy at q_c.

Our study shows that the mismatch degree induced hydride redirection is mainly dominated by the relative magnitude of the elastic energy in the horizontal and vertical directions. The redirection behaviour persists even when the effects of temperature and interfacial energy are taken into account. These insights provide valuable contributions to our understanding of how interfacial coherency loss impacts the morphology of δ-hydrides.

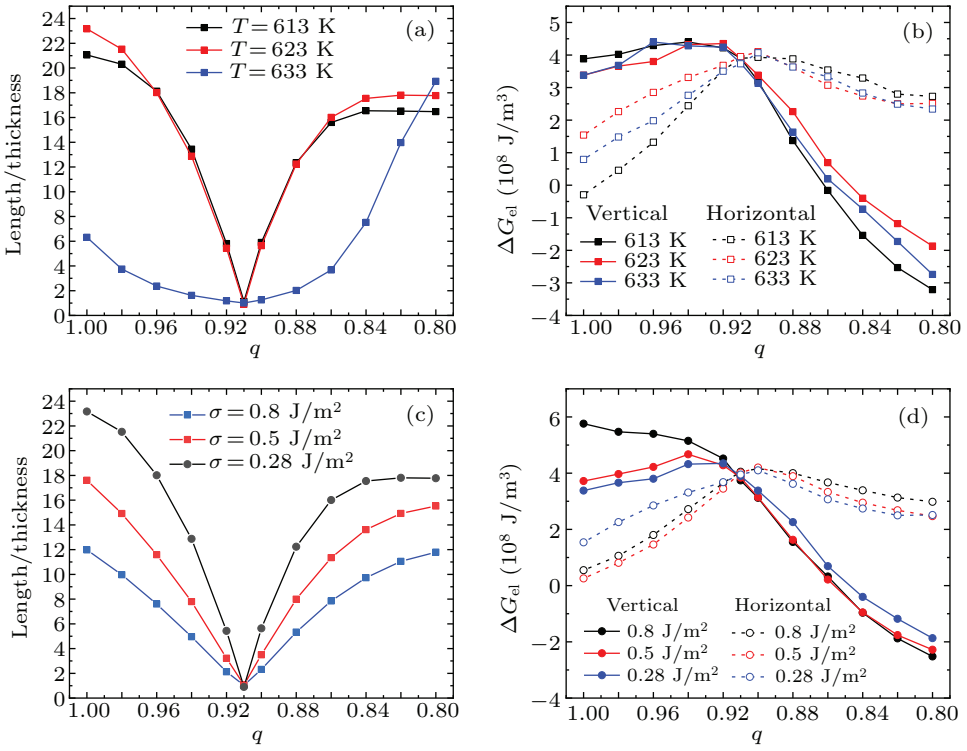


Fig. 8. (a) The length-to-thickness ratio of hydrides at different temperatures and mismatch levels, (b) elastic interaction energy in horizontal and vertical directions at different temperatures and mismatches, (c) the length-to-thickness ratio of hydrides at different interfacial energies and mismatch levels, (d) elastic interaction energy in horizontal and vertical directions at different interfacial energies and mismatches.

4. Conclusion

In this study, the PF method was used to investigate the influence of temperature and interfacial effects on the kinetic process of hydrides formation. By constructing two-phase free energy curves at different temperatures using the CALPHAD thermodynamic approach, the following main results were observed:

(i) In the zirconium alloy cladding service temperature range, temperature and interfacial conditions can indeed impact the length-to-thickness ratio and growth rate. The length-to-thickness ratio of hydrides first increase and then decrease as the temperature rises. The increase of interfacial energy results in the decrease of the length-thickness ratio of the hydrides. Additionally, the growth rate of hydrides demonstrates a decrease with an increase in temperature and interfacial energy.

(ii) The loss of interfacial coherency has a dual effect, not only affecting the length-to-thickness ratio and average growth rate of the hydrides, but also leading to redirection behaviour and an increase in the maximum stress value at the hydrides tip. As interfacial coherency loss increases, the hydrides length-to-thickness ratio initially decreases ($q > q_c$) and subsequently increases ($q < q_c$), accompanied by an initial decrease and subsequent increase in the average growth rate. This phenomenon can be attributed to the anisotropic distribution of elastic interactions caused by the loss of interfacial coherency. Interestingly, the reorientation of hydrides at the mismatch degree q_c remains unaffected by temperature and changes in interfacial energy.

By presenting these results, this investigation enhances our understanding of the growth patterns and dynamic evolution of Zr hydrides as influenced by temperature and interfacial effects. Nevertheless, it is important to acknowledge that the above-mentioned conclusions are based on the assumption of

elastic and isotropic interfacial energy, and the effects of plastic and anisotropic interfacial energy will be considered in the future.

Acknowledgements

We thank Yuan-Ji Xu, Bei-Lei Liu, Jin-Xiang Wang, Kai-Le Chen, Bo-Hao Zhao, Yu Song, and Jing Wang for helpful discussions. Project supported by the National Natural Science Foundation of China (Grant Nos. U2230401, U1930401, and 12004048), the National Key Research and Development Program of China (Grant No. 2021YFB3501503), the Science Challenge Project (Grant No. TZ2018002), and the Foundation of LCP. We thank the Tianhe platforms at the National Supercomputer Center in Tianjin.

References

[1] Hedayat A 2017 *Nuclear Engineering and Design* **313** 190
[2] Bair J, Zaeem M A and Tonks M 2015 *J. Nucl. Mater.* **466** 12
[3] Motta A T, Capolungo L, Chen L Q, Cinbiz M N, Daymond M R, Koss D A, Lacroix E, Pastore G, Simon P C A, Tonks M R, *et al.* 2019 *J. Nucl. Mater.* **518** 440
[4] Ensor B, Lucente A, Frederick M, Sutli J and Motta A 2017 *J. Nucl. Mater.* **496** 301
[5] Ghosal S, Palit G and De P 2001 *Mineral Procesing and Extractive Metallurgy Review* **22** 519
[6] Kim S, Kang J H and Lee Y 2022 *J. Nucl. Mater.* **559** 153393
[7] Zuzek E, Abriata J, San-Martin A and Manchester F 1990 *Bulletin of Alloy Phase Diagrams* **11** 385
[8] Daum R, Chu Y and Motta A 2009 *J. Nucl. Mater.* **392** 453
[9] Puls M P 2012 *The effect of hydrogen and hydrides on the integrity of zirconium alloy components: delayed hydride cracking* (Springer Science & Business Media)
[10] Han G, Zhao Y, Zhou C, Lin D Y, Zhu X, Zhang J, Hu S and Song H 2019 *Acta Materialia* **165** 528
[11] Heo T W, Colas K B, Motta A T and Chen L Q 2019 *Acta Materialia* **181** 262
[12] Colas K, Motta A, Almer J, Daymond M, Kerr M, Banchik A, Vizcaino P and Santisteban J R 2010 *Acta Materialia* **58** 6575
[13] Colas K, Motta A, Daymond M, Kerr M and Almer J 2010 *Journal of ASTM International* **8** 1
[14] Colas K B, Motta A T, Daymond M R and Almer J D 2013 *J. Nucl. Mater.* **440** 586
[15] Kwon Y, Thornton K and Voorhees P W 2007 *Phys. Rev. E* **75** 021120
[16] Seol D, Hu S, Li Y, Shen J, Oh K and Chen L 2003 *Metals and Materials International* **9** 61
[17] Kwon Y, Thornton K and Voorhees P 2009 *Europhys. Lett.* **86** 46005
[18] Mendoza R, Savin I, Thornton K and Voorhees P 2004 *Nat. Mater.* **3** 385
[19] Boettinger W J, Warren J A, Beckermann C and Karma A 2002 *Annual Review of Materials Research* **32** 163
[20] Yang C, Li S, Wang X, Wang J and Huang H 2020 *Comput. Mater. Sci.* **171** 109220
[21] Yang C, Liu Y, Huang H, Wu S, Sheng J, Shi X, Wang J, Han G and Song H 2021 *Mater. Res. Express* **8** 106518
[22] Wang Y U, Jin Y M and Khachaturyan A G 2004 *Acta Mater.* **52** 81
[23] Shi X, Wang J, Xu J, Cheng X and Huang H 2022 *Acta Mater.* **237** 118147
[24] Shi X, Wang J, Cheng X and Huang H 2022 *Advanced Theory and Simulations* **5** 2100345
[25] Shi X, Wang J, Cheng X and Huang H 2022 *Physica Status Solidi (RRL)-Rapid Research Letters* **16** 2100416
[26] Zhao Z, Blat-Yrieix M, Morniroli J, Legris A, Thuinet L, Kihn Y, Ambard A, Legras L, Limback M, Kammenzind B, *et al.* 2008 *Characterization of zirconium hydrides and phase field approach to a mesoscopic-scale modeling of their precipitation* (ASTM International)
[27] Thuinet L, De Backer A and Legris A 2012 *Acta Mater.* **60** 5311
[28] Thuinet L, Legris A, Zhang L and Ambard A 2013 *J. Nucl. Mater.* **438** 32
[29] Ma X, Shi S Q, Woo C and Chen L 2002 *Scripta Materialia* **47** 237
[30] Ma X, Shi S Q, Woo C and Chen L 2002 *Mater. Sci. Eng. A* **334** 6
[31] Ma X, Shi S Q, Woo C and Chen L 2002 *Computat. Mater. Sci.* **23** 283
[32] Ma X, Shi S Q, Woo C and Chen L 2006 *Mechanics of Materials* **38** 3
[33] Shi S Q and Xiao Z 2015 *J. Nucl. Mater.* **459** 323
[34] Bair J, Zaeem M A and Tonks M 2016 *J. Phys. D: Appl. Phys.* **49** 405302
[35] Jokisaari A and Thornton K 2015 *Calphad* **51** 334
[36] Bair J, Zaeem M A and Schwen D 2017 *Acta Mater.* **123** 235
[37] Lin J l and Heuser B J 2019 *Comput. Mater. Sci.* **156** 224
[38] Shin W and Chang K 2020 *Comput. Mater. Sci.* **182** 109775
[39] Simon P C, Aagesen L K, Jokisaari A M, Chen L Q, Daymond M R, Motta A T and Tonks M R 2021 *J. Nucl. Mater.* **557** 153303
[40] Wu S, Sheng J, Yang C, Shi X, Huang H, Liu Y and Song H 2022 *Frontiers in Materials* **9** 916593
[41] Kim S G, Kim W T and Suzuki T 1999 *Phys. Rev. E* **60** 7186
[42] Steinbach I and Apel M 2006 *Physica D* **217** 153
[43] Dupin N, Ansara I, Servant C, Toolon C, Lemaignan C and Brachet J 1999 *J. Nucl. Mater.* **275** 287
[44] Zhong Y and Macdonald D D 2012 *J. Nucl. Mater.* **423** 87
[45] Sheng J, Wang Y C, Liu Y, Wu S, Xu K, Chen Z H, Sun B, Liu H F and Song H F 2022 *Comput. Mater. Sci.* **213** 111663
[46] Sheng J, Liu Y, Shi X M, Wang Y C, Chen Z H, Xu K, Wu S, Huang H B, Sun B, Liu H F and Song H F 2024 *Comput. Mater. Sci.* **235** 112779
[47] Mai W, Soghrati S and Buchheit R G 2016 *Corrosion Science* **110** 157
[48] Yang C, Huang H, Liu W, Wang J, Wang J, Jafri H M, Liu Y, Han G, Song H and Chen L Q 2021 *Adv. Theor. Simul.* **4** 2000162
[49] Morris Jr J 2010 *Phil. Mag.* **90** 3
[50] Lubliner J 2008 *Plasticity theory, revised* edn.
[51] Louchez M A, Thuinet L, Besson R and Legris A 2017 *Comput. Mater. Sci.* **132** 62
[52] Zhang Y, Bai X M, Yu J, Tonks M R, Noordhoek M J and Phillpot S R 2016 *Acta Mater.* **111** 357
[53] Olsson P, Massih A, Blomqvist J, Holston A M A and Bjerken C 2014 *Comput. Mater. Sci.* **86** 211
[54] Porter D A and Easterling K E 2009 *Phase transformations in metals and alloys* (revised reprint) (CRC press)
[55] Steinbrück M, Birchley J, Boldyrev A, Goryachev A, Grosse M, Haste T, H ozer Z, Kisselev A, Nalivaev V, Semishkin V, *et al.* 2010 *Prog. Nucl. Energy* **52** 19
[56] Jokisaari A M 2016 *Multiphysics Phase Field Modeling of Hydrogen Diffusion and δ-Hydride Precipitation in α-Zirconium* (Ph.D. thesis)
[57] Massih A R and Jernkvist L O 2009 *Comput. Mater. Sci.* **46** 1091
[58] Liu S M, Ishii A, Mi S B, Ogata S, Li J and Han W Z 2022 *Small* **18** 2105881